Tuning the Electronic Properties of γ-Al2O3 Surface by Phosphorus Doping

Journal:	*Physical Chemistry Chemical Physics*
Manuscript ID	CP-ART-05-2019-003105
Article Type:	Paper
Date Submitted by the Author:	31-May-2019
Complete List of Authors:	Acikgoz, Muhammed; Rutgers University Newark, Chemistry Khoshi, Reza Amir; Rutgers University Newark, Chemistry Harrell, Jaren; Rutgers University Newark Faculty of Arts and Sciences Genova, Alessandro; Rutgers University Newark, Chemistry Chawla, Rupali; Rutgers University Newark Faculty of Arts and Sciences He, Huixin; Rutgers University, Department of Chemistry Pavanello, Michele; Rutgers University, Chemistry; Rutgers University Newark, Chemistry

SCHOLARONE™
Manuscripts

Tuning the Electronic Properties of γ-Al_2O_3 Surface by Phosphorus Doping

Muhammed Acikgoz[*], M. Reza Khoshi[*], Jaren Harrell, Alessandro Genova, Rupali Chawla, Huixin He[†], and Michele Pavanello[‡,]**

Department of Chemistry, Rutgers University, Newark, NJ 07102

ABSTRACT

Tuning the electronic properties of oxide surfaces is of pivotal importance, because they find applicability in a variety of industrial processes, including catalysis. Currently, the industrial protocols for synthesizing oxide surfaces are limited to only a partial control on the oxide's properties. That is because the ceramic processes result in complex morphologies and *a priori* unpredictable behavior of the products. While the bulk doping of alumina surfaces has been demonstrated to enhance their catalytic applications (i.e. hydrodesulphurization (HDS)), the fundamental understanding of this phenomenon and its effect in atomic level remains unexplored. In our joint experimental and computational study, simulations based on Density Functional Theory (DFT), synthesis, and a variety of surface characterization techniques are exploited for the specific goal of understanding the structure-function relationship of Phosphorus-doped γ-Al_2O_3 surfaces. Our theoretical calculations and experimental results agree in finding that P doping of γ-Al_2O_3 leads to a significant decrease in its work function. Our computational models show that this decrease is due to the formation of a new surface dipole, providing a clear picture of the effect of P doping at the surface of γ-Al_2O_3. In this study we uncover a paradigm for tuning support-catalyst interaction that departs from details of the chemistry and intimately involves the electrostatic properties of the doped γ-Al_2O_3 surface specifically, the surface dipole. Our findings open a new pathway for engineering the electronic properties of metal oxides' surfaces.

Keywords: Catalysis; Gamma alumina; Density functional theory (DFT); Nanoparticles; Work function; Surface dipole.

---

[*] These authors contributed equally to the work.

[**] Also affiliated in Physics Department.

[†] huixinhe@rutgers.edu

[‡] m.pavanello@rutgers.edu

INTRODUCTION

Metal oxides and their surfaces find extensive use in numerous fields of materials science, such as chemical catalysis, photocatalysis, and photovoltaics, among others.[1,2] Thus, engineering the electronic properties of the oxide surfaces is crucial for a broad application of the materials, as well as for the improvement of their current applications.[1,3] As of today, however, serious limitations affect the extent of this control, mainly for two reasons. First, most synthetic methods yielding well defined doped surfaces are limited to academic use (small scale)-which are not cost effective for industrial applications - or the products are not stable in those operational conditions of most industrial processes.[4] Secondly, the ceramic processes typically employed in industry to engineer oxide-containing materials result in complex morphologies[5] and *a priori* unpredictable behavior of the generated materials.

In this work, our primary goal is to generate phosphorous doped alumina surfaces, by employing simple ceramic processes and characterizing their electronic properties. We aim at shedding light on three major points: (1) theory-experiment correlation to inspect the average or the most likely surface morphology (we consider an array of possible location of P on γ-Al_2O_3 surfaces); (2) finding a structure-function relationship between the electronic properties and surface morphology. This can be exploited when metal oxides are engineered; (3) determining the degree of stability for various possible surface terminations, as well as P locations in the P-doped γ-Al_2O_3 (P-γ-Al_2O_3).

Our study focuses on an atomic-level understanding of the morphology and the structure-property relationships of realistic (hydroxylated) surfaces of P-γ-Al_2O_3 nanoparticles. γ-Al_2O_3 has been widely used as adsorbent and catalysts,[6] and also it is perhaps the most important nanomaterial used as a support for metal catalysts.[7] The properties of Al_2O_3 can change during chemical operations, which include chemical contamination, thermal stress leading to loss of surface area, pore blockage, and undesired crystal phases.[8,9,10] It has been empirically observed that dopants improve the overall performance of catalysts acting as crystal phase and/or surface area stabilizers.[11,12,13] For example, studies have been reported that treating the surface of γ-Al_2O_3 with phosphates could largely promote the performance of the catalysts in hydrodesulphurization (HDS).[13,14,15] Also, doping of γ-Al_2O_3 is commonly used for tuning its mechanical[16,17] and optical properties.[18,19] Many dopants such as metal, silica, and heteroatoms, have been used to modify the surface and bulk γ-Al_2O_3 during fabrication.[20,21,22,23] Phosphorus is our choice of dopant, because it has variety of atomic coordinations and multiple electronic states. Also, it is known that phosphorus can covalently bind to Al_2O_3, thus making a stable catalyst support.[24,25]

Experimentally, we characterized the structural and chemical properties of both P-doped and non-doped γ-Al_2O_3 nanoparticles by utilizing Fourier transform infrared spectroscopy (FT-IR), solid-state magic-angle spinning nuclear magnetic resonance (MAS-NMR), energy-dispersive X-ray spectroscopy (EDS), and Peak Force Kelvin probe force microscopy (PF-KPFM) techniques. On the theoretical side, we carried out several DFT simulations accounting for an array of surface and doping morphological models. Electronic properties were characterized by computing the density of Kohn-Sham states (DOS), surface work function and surface dipole moment; as well as IR and NMR of P-doped and non-doped γ-Al_2O_3.

RESULTS AND DISCUSSION

To investigate the P content in the doped γ-Al_2O_3 structure, EDS was conducted, using EDAX coupled with FE-SEM Hitachi S-4800. As EDAX microprobe analysis is semi-quantitative, analysis of several samples was carried out and averaged values are presented in **Table 1**.

Element	Weight%	Atomic%
O	42.8	56.2
Al	48.7	38.0
P	8.5	5.8

Table 1. The results of EDS analysis for the P- γ-Al_2O_3 samples.

We perform DFT calculations (see the Computational details section) where γ-Al_2O_3 and P-γ-Al_2O_3 surfaces are presented for two different essential surface models, namely oxygen terminated and 100% hydroxylated (OH terminated). We considered single-atom doping as well as two-atom doping (i.e., two interacting and independent P atoms in the simulation cell). Each structure underwent geometry optimization. Although we carried out the simulations on two cell sizes (a small bulk unit containing 40 atoms and a supercell containing 160 atom bulk) the presented results are based on the simulations of the larger, more realistic cell, unless otherwise stated. Both slab models consist of five cation layers (tetrahedrally and octahedrally coordinated Al atoms). A vacuum thickness of 15 Å above the surface was added between two periodically repeated slabs. We placed P on one surface of the slab. The bottom 40% of atoms in each slab was kept fixed at their optimized positions throughout the simulations. We consider four different positions for the P atoms in two categories:

- models **sub/surf**: P locates to a subsurface/surface site substituting an Al atom;
- models **md/bd**: P is in a phosphate-type ligand with mono/bidentate complexation to a surface Al atom;

Throughout the manuscript, we use abbreviations to identify each surface model of the relevant termination (e.g., **O-sub** and **OH-sub** are for subsurface location of P on O-terminated and OH-terminated surfaces, respectively).

In the simulation, we choose the (001) surface of γ-Al_2O_3 in the spinel-like bulk morphology proposed by Gutierrez et al[26], Pinto et al[27], and Taniike et al.[28] This structure compares favorably to known crystallographic and physical properties of γ-Al_2O_3.[29] In **Figure**

1 we depict the computed morphology (**a** and **b**) for the O-terminated γ-Al_2O_3 model as well as its associated DOS, plot (**c**). Not surprisingly, this surface termination activates the material. Although it is known that this termination is only detectable at very high temperatures, we present it here as a model for Oxygen-rich surface islands.

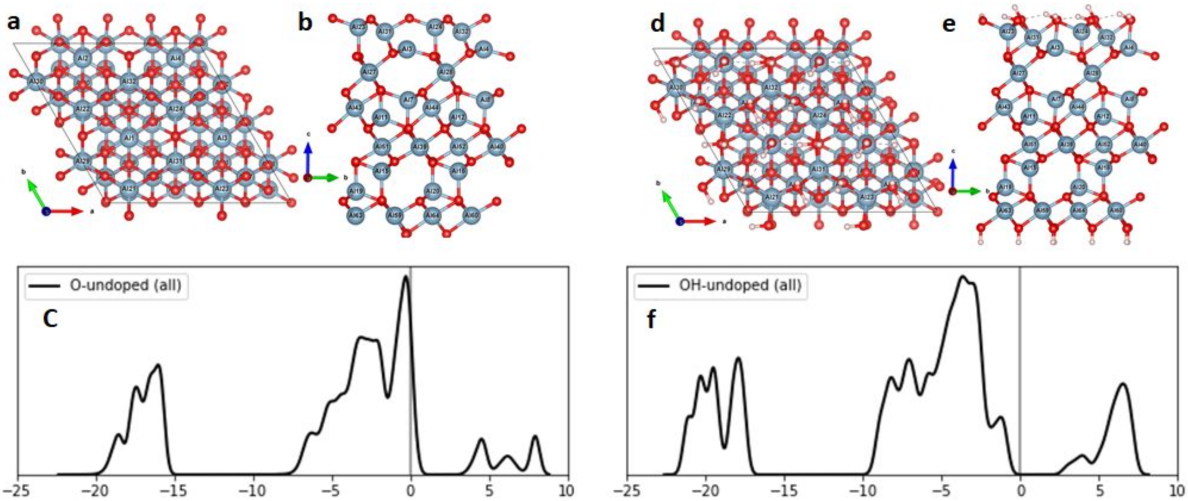

Fig. 1. Computed morphology, both top view (**a**) and side view (**b**), and associated DOS (**c**) of non-doped O terminated γ-Al_2O_3 surface. Those of the 100% hydroxylated γ-Al_2O_3 surface are given in (**d**), (**e**), and (**f**), respectively. Fermi energy placed at zero for DOSs.

As our picture of γ-Al_2O_3 is that of a heterogeneous material with OH-rich and O-rich domains, we also present a depiction of the 100% hydroxylated surface termination of the supercell in **Figure 1** (**d** and **e**) alongside the associated DOS plot (**f**). From the mentioned figure, it is clear that, as expected, hydroxylated γ-Al_2O_3 is an insulator and electronically stable.

Experimentally, the P-doped γ-Al_2O_3 was synthesized by impregnation of phosphoric acid and commercially available γ-Al_2O_3, followed by a simple and commonly applied ceramic process, i. e. high temperature annealing process in air (see the experimental details section). By optimizing the ratio of γ-Al_2O_3 and the molarity of H_3PO_4, we are able to tune the doping level of P. In **Figure 2** we show the atomic-level surface morphologies, resulted from the DFT simulations and the corresponding PDOS. When considering phosphate chemisorption, it can be realized through a monodentate or bidentate ligand configuration. Additionally, here we consider two types of slabs: one that is stoichiometric with a P(+5) oxidation state, and one that is consistent with a P(+3) oxidation state. This was accomplished by the addition of an electron donor to the bottom of the slab. The relevant computed morphologies and associated PDOSs can be seen in **S1** and **S2** for both O-terminated and OH-terminated surface models, where it can be seen that the phosphorous coordination and overall local geometry and surface PDOS are slightly affected by the overall stoichiometry of the slab. This indicates that the chosen slab model is sufficiently thick that the surface properties are resilient to the chemistry occurring at the other end of the slab.

In the models **O-sub**/**O-surf** and **OH-sub**/**OH-surf**, the doping P atom was introduced at a tetrahedral Al site. The theoretical prediction delivers a clear picture for **O-sub**: a planar configuration is assumed for P consistent with an effective double oxidation (+3 oxidation state). For this model, we also explore the O terminated subsurface doped with two P atoms at the three tetrahedral doping sites (**Figures S3** and **S4)**. The three resulting models show how the location of the second P atom introduces significant changes to the shape of the conduction band (CB). As there are unoccupied orbitals with P character, therefore similarly to the previous O terminated P-doped model (**O-sub**) one or both subsurface P atoms have +3 oxidation state character. When the P atom is located on the surface (model **O-surf**), it causes surface reorganization and distortions across the surface O atoms to form an O-dimer (see the relevant structure in **Figure 2a**). The computed PDOS of this model has a band gap of 4 eV and it shows that the Fermi level lies at the top of the valence band. The computed PDOS plots display no significant changes either in monodentate (**O-md**) or bidentate (**O-bd**) configuration models, even though the surface morphology in **O-bd** was affected by several distortions of surface O atoms.

A

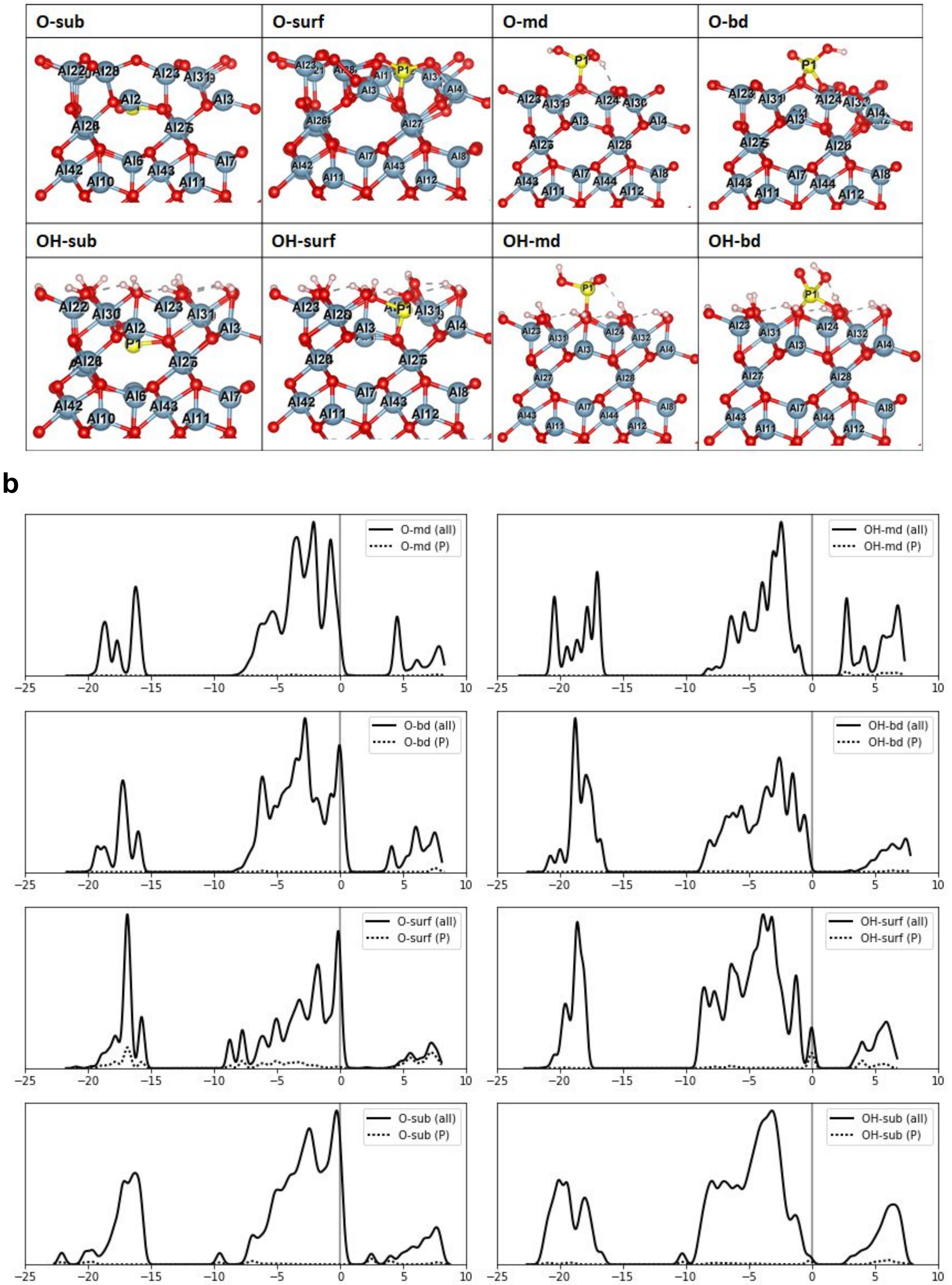

Fig. 2. Models of O terminated and OH terminated P-γ-Al_2O_3 surfaces (**a**) and their associated surface PDOSs (**b**). The P atom is placed at various positions as defined before, particularly at the spinel defect site for **O-sub** and **OH-sub** models. In the PDOSs, the Fermi energy is set to zero. A clearer depiction of the tri-coordinated P atom in O-surf of inset (a) is found in **Figure S6**.

When doping the OH terminated surface, we obtain the morphology/DOS depicted in **Figure 2**. In model **OH-sub**, the P atom is now non-planar, maintaining the lone pair as a partially filled state. At the same time, the P atom is sheltered in a sub-surface site. The surface P atom doping (**OH-surf** model) at the tetrahedral Al site causes the neighboring octahedral Al to become five coordinated. In this situation, the surface P atom becomes three coordinated (see **Figure S5**). When considering the phosphate models (**OH-md** and **OH-bd**), we notice that the surface largely maintains its non-doped surface morphology (low reorganization), but the DOS profile changes, displaying clear gaps with no P states on the band edges.

We further investigate the subsurface P doping and also consider higher concentration doping (i.e., two independent P atoms in the same simulation cell). The idea behind this set of simulations is to inspect the extent of nonadditivity/cooperation in the electronic behavior of the surfaces after P-doping. We achieved this by replacing another tetrahedral Al with P. The second P was inserted at three of the different, available and inequivalent tetrahedral Al locations and considered both the OH and O terminated surfaces. For the OH terminated surface, we found two local minima of the potential energy surface. The first structure features one P atom four-coordinated with three subsurface oxygen atoms and one surface hydroxyl group. The second P location is 3 coordinated with its lone pair still on P and pointing in the direction of the spinel defect site (**Figure S6a**). In the second local minimum structure, the P closer to the surface moved toward the bulk expelling a water molecule (**Figure S6b**). When the O-terminated surface is considered, the two P atoms achieve a planar tri-coordinated geometry. Conceivably, this is an indication that the oxidation state of P atoms is now +3.

The PDOS of these surfaces showed largely the same trend as for singly-doped surfaces. For the O-terminated surfaces, P doping induces a narrowing of the gap and the appearance of states with P character at the band edges. The OH-terminated surfaces are more resilient to the doping and maintain a large gap. However, as for the case of the singly-doped surface, the valence band (VB) edge has a strong P character (**Figure S7**). Thus, we do not find a significant cooperative effect between P sites.

Our next set of investigations regard the simulations and measurement of the work function (WF or ϕ) of P doped and non-doped γ-Al_2O_3 nanoparticles. To understand the influence of P doping on the work function of γ-Al_2O_3 nanoparticles, PeakForce Kelvin probe force microscopy (PF-KPFM™) in an Argon-filled glovebox is conducted for both doped and non-doped γ-Al_2O_3 nanoparticles (see **S8** for more details). PF-KPFM measurement is carried out on several nanoparticles with similar dimensions for each sample (**Figure 3**).

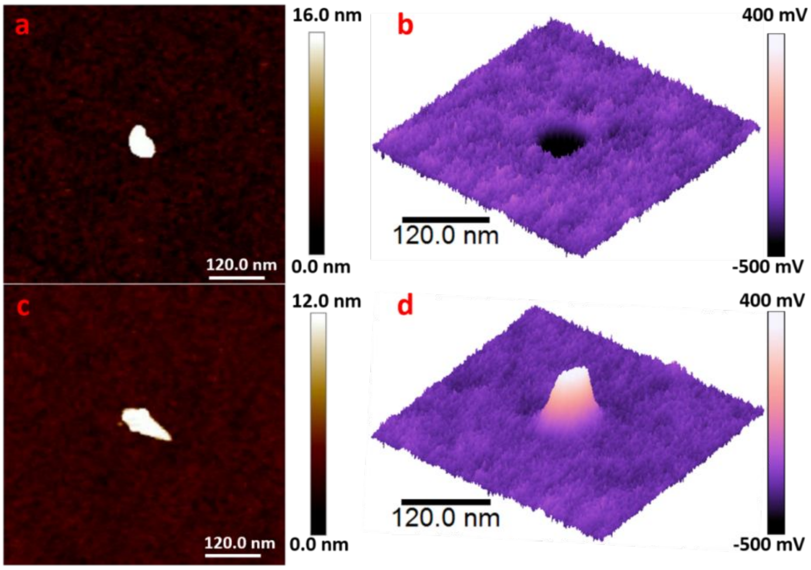

Fig. 3. (A and C) Topography and (B and D) potential mapping images of γ-Al_2O_3 and P-γ-Al_2O_3, respectively.

The average measured WF of the γ-Al_2O_3 is 4.88±0.04 eV, while the average measured WF of P-γ-Al_2O_3 is 4.16±0.06 eV. Our results show that doping of γ-Al_2O_3 by phosphorus, has lowered its WF by almost 15% (**Figure 4a**).

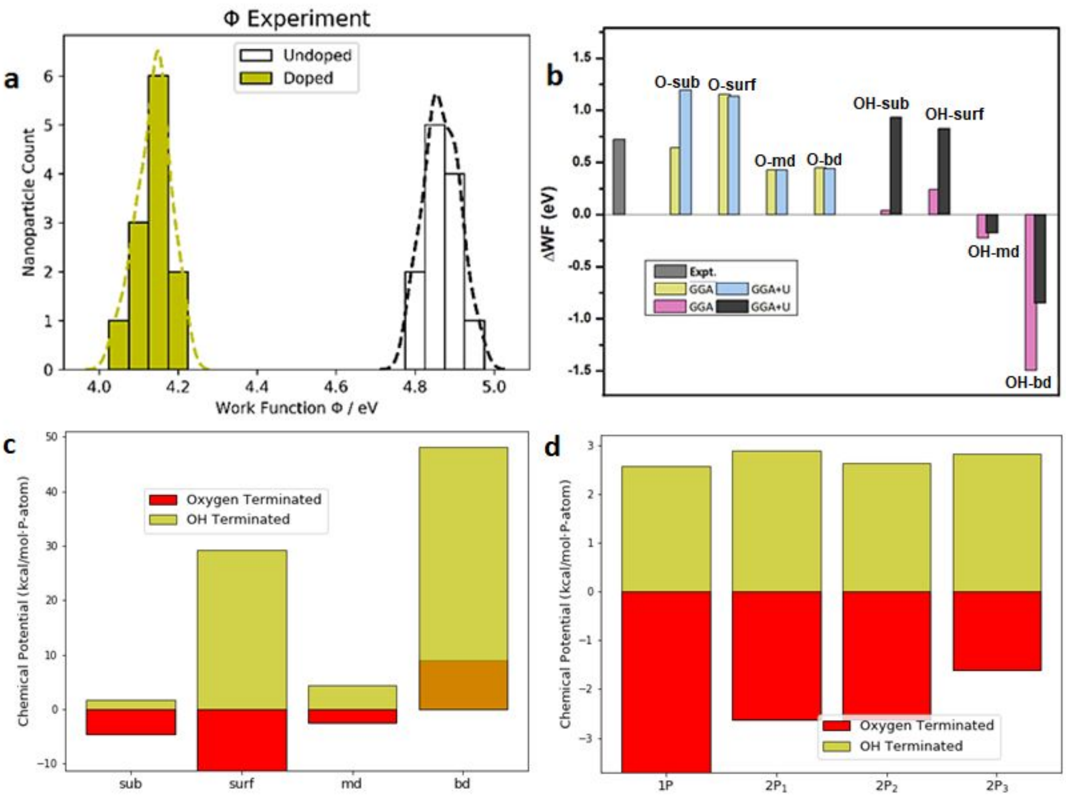

Fig. 4. (**a**) Experimentally determined WFs for non-doped and P-doped γ-Al_2O_3. (**b**) Comparison of the experimentally and theoretically determined WF differences (ΔWF) between non-doped and P-doped structures for supercell models of O-terminated and OH-terminated surfaces. Here, the negative ΔWF denotes the increase in WF after P-doping as opposed to experimental results. (**c**) Surface stability diagram of P doping in terms of the chemical potential for both O-terminated and OH-terminated surfaces. (**d**) Surface stability diagram of P doping (**O-sub** and **OH-sub** models) in terms of the chemical potential. $2P_1$, $2P_2$, and $2P_3$ are for three different available tetrahedral Al sites.

We employ and compare GGA with GGA+U for the calculation for the WFs of all surface models. In performing GGA+U we derive suitable U values for O (1.11 eV) and P (1.77 eV) by employing the Cococcioni-de Gironcoli linear response method[30] to the small surface structures (40 atoms). DFT+U is chosen here to remove the spurious self-interaction present in semilocal (GGA) exchange-correlation functionals[31] and is particularly suited to improve the *ab-initio* description of surfaces and interfaces.

The corresponding surface-averaged electrostatic potential of each model are plotted as a function of distance from the surface (figures in **S9**). The values of WFs and corresponding surface dipole contributions (ϕ_d) are presented and compared with GGA quantities (see **Table S1** for the entire set of calculated values).

It is seen that for all surface models except **OH-md** and **OH-bd**, the computed WFs agree with the experiment in that WF is reduced as a result of P-doping. The reason for the fact that **OH-md** and **OH-bd** models stand out is complex and it involves two observations: (1) the surfaces do not rearrange significantly from the non-doped case, and (2) the P-OH contribution to the surface dipole is to increase it. Specifically, comparing the P-OH angle and OH direction in **O-md** and **O-bd** with the OH- counterparts from **Figure 2**, we notice that the hydroxylated surfaces see a P-OH pointing upward, while the O-terminated surfaces see a P-OH pointing downward. Thus, when the phosphates are added to the surface, the dipole is depleted for the O-terminated surfaces and enhanced for the OH-terminated ones. This observation is especially important for the **OH-bd** system. When we inspect the effect of doping by two independent P atoms (higher concentration) on the WF for the various structures of subsurface (**O-sub** and **OH-sub**) models (see the chart in **S10a**), we notice that the addition of the second P atom further decreases the WF. Thus, theory and experiment semiquantitatively agree that on average P-γ-Al_2O_3 has a lower WF than non-doped γ-Al_2O_3, with the chemisorbed phosphate models going against the trend and increasing the WF values when the OH-terminated surfaces are considered.

To understand the reasons for the WF reduction by P doping we present in **Figure 4b** the WF differences ($\Delta\phi$) between the non-doped and P-doped surfaces of each structural model, providing us with a comparison of theory and experimental results. It shows that all the O-terminated surfaces are in accordance with the experiment by yielding lower WF after P-doping (**Figure 4b**). Whereas, the dentate models (**OH-md** and **OH-bd**) increase WF values.

The size of the surface dipole contribution to ϕ (ϕ_d) estimated by computing the difference between the left and right vacuum levels[32] exhibits a clear trend that ϕ_d reduces linearly with the increase in the number of P dopant for the O-terminated surfaces whereas it conversely rises for the OH-terminated surfaces (see **Figure S10b**).

Our analysis is substantiated by characterizing the energetic stability of the O-/OH-terminated surfaces in terms of chemical potentials, μ, (see **Figure 4c**) reveal that dentate attachment models on both O- and OH-terminated surfaces (**O-md/OH-md** and **O-bd/OH-bd**) are quite less stable compared to other surface models (**O-sub/OH-sub** and **O-surf/OH-surf**). Also, O-terminated surfaces are more stable than OH-terminated ones by providing **O-sub** models as the most stable ones among all possible configurations (**Figure 4d**).

Furthermore, to get a structure-function relationship among various surface models of P-γ-Al_2O_3 discussed here, we plot a correlation between the WF and ϕ_d (**Figure S11**), which demonstrate the behavior of the electronic structure against the various P location on γ-Al_2O_3 surfaces. **Figure S11a** shows that there exists a clear linear correlation between ϕ and ϕ_d for the models of O-terminated surfaces, whereas less correlation for ϕ- ϕ_d occurs for OH-terminated surfaces of supercell (**Figure S11b**). However, the similar plots for the small cell models (**O-** and **OH-**) (see **Figure S11c&d**) display a less linear correlation for O-terminated surfaces but a relatively good correlation for OH-terminated ones. This shows the importance of sizable finite size effects and surface relaxation effects on modeling of γ-Al_2O_3 surfaces. [33] Upon inspection of the Bader charges of the P atom in O-terminated and OH-terminated surfaces, all varying between 0.14 and 0.17, we further confirm that the reduction in the WF witnessed in our simulations is due to a change in dipole moment orientation rather than to charge transfer.

In order to obtain more detailed information about the structure and change in the chemical environment after P doping, the Al-NMR spectra were obtained for three samples; the as received γ-Al_2O_3, P doped γ-Al_2O_3 and heated γ-Al_2O_3, which was obtained by annealing the γ-Al_2O_3 at the same temperature as applied for P doped γ-Al_2O_3, just without H_3PO_4 source. (**Figure 5a**). The spectrum of as-received γ-Al_2O_3 sample (in black) shows two peaks which are corresponding to AlO_4 at around 70 ppm and to AlO_6 around 12 ppm with an about 1:2 integration ratio, which is consistent with the literature reported values.[34,35,11] In the case of P-γ-Al_2O_3, the peak positions for AlO_6 and AlO_4 remain unchanged. While a new sharp peak appeared at 42.3 ppm and a shoulder to the octahedral Al peak at around 4 ppm. The peak at 42.3 ppm has been assigned to AlO_5 bonding. It is worth to mention that the AlO_5 surface units have been considered as selective anchoring sites for Pt catalysts.[34] The upshifted shoulder is possibly caused by the coupling of P with the AlO_6 units to form Al-O-P in the local environment of the surface AlO_6 units.[11]

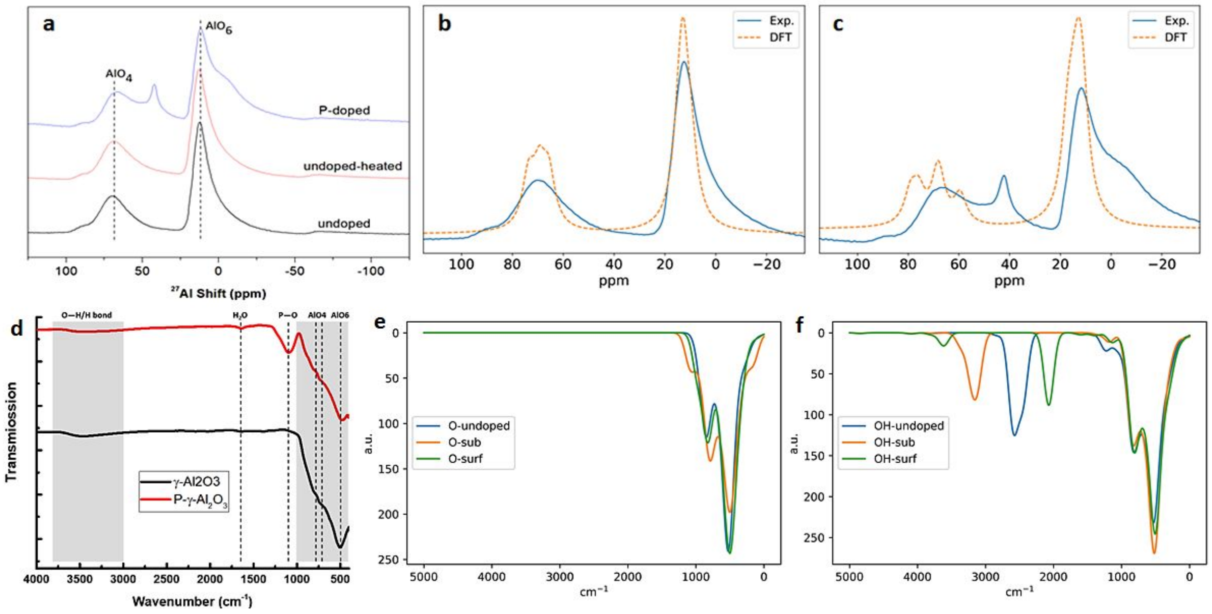

Fig. 5. (**a**) ^{27}Al magic-angle spinning (MAS) NMR spectra of P-γ-Al_2O_3 (top), heated γ-Al_2O_3 (middle), and as received γ-Al_2O_3 (bottom). Theoretical predictions of solid-state Al-NMR spectra computed on a bulk model supercell including 40 independent atoms and plotted with dashed lines; (**b**) Non-doped γ-Al_2O_3, (**c**) P-doped γ-Al_2O_3. (**d**) Experimental IR spectra of the non-doped and P-doped γ-Al_2O_3 nanoparticles. Calculated IR spectra (**e**) for subsurface (**O-sub**) and surface (**O-surf**) P-doped O-terminated surface models and (**f**) for subsurface (**OH-sub**) and surface (**OH-surf**) P-doped OH-terminated surface models.

To assure that these structural changes are not due to a simple high temperature annealing effect, a control experiment was conducted, where the as-received γ-Al_2O_3 was heated to 550^{o}C for 4.5 hrs (the same heating condition as in P-doping process, without the phosphorus source). As shown in **Figure 5a**, the heated γ -Al_2O_3 shows the similar NMR spectrum to the as-received one, [34] suggesting that the P-doping process promoted the structural rearrangement for the formation of so-called pentahedral coordination units (AlO_5) and possible Al-O-P structures.

Additional evidence supporting the experimental measurements for Al-NMR is provided by the theoretical calculations. Computations of bulk γ-Al_2O_3 (carried out with GIPAW[36] on bulk γ- Al_2O_3), reproduce the experimental spectrum of the clean non-doped γ-Al_2O_3 nanoparticles with remarkable accuracy (**Figure 5b**). The computational spectra (**Figure 5c**) assign the peak at 42.3 ppm to either distorted tetrahedral or distorted octahedral-coordinated Al atoms. Our work, thus, improves upon recent theoretical results[37] which could only tentatively assign the 42.3 ppm peak to pentacoordinated Al atoms. We further find that the pentacoordinated Al atoms, depending on the nature of the bonding (length and angles) give rise to NMR peaks upfield (not shown) compared to the octahedral Al atoms explaining the presence of the shoulder peak. It should be noted that our DFT calculations for the NMR of the P-doped surface structures did not converge. Our works regarding a comprehensive NMR computation of P-doped γ-Al_2O_3 surface structures to accurately understand the shoulder at 0 ppm and the additional sharp peak at 42.3 ppm are in progress and will be published elsewhere.

To gain more informaion about the chemical bonds, both non-doped and P-doped γ-Al_2O_3 nanoparticles were characterized with FT-IR spectroscopy (**Figure 5d**). Also, we computed the vibrational frequencies for the models of O-terminated (**Figure 5e**) and OH-terminated (**Figure 5f**) γ-Al_2O_3 surfaces. The experimental spectrum of γ-Al_2O_3 show a wide peak between 3000-3800 cm^{-1} , which is assigned to O-H stretching and the hydrogen bond between the OH groups existing on the surface of Al_2O_3. [38,39] The computational spectra of all OH-terminated surface models and dentate models of O-terminated surfaces (**O-md** and **O-bd**) confirmed that the peaks in this region are due to asymmetric stretching mode of O-H (see **Figure 5f** and **Figure S12a&b**). The EDAX measurement indicated that the P loading in the P-γ-Al_2O_3 was around wt. 8.5% (atomic 5.6%), which is much higher than those required to react all the surface hydroxy groups on the surface of γ-Al_2O_3. [40,41] However, this peak still exists, eventhough it is weakened in P-γ-Al_2O_3. At the same time, the peak intensity is increased in P-γ-Al_2O_3 at 1639 cm^{-1}, which has been assigned as the bending moment of adsorbed water molecules.[42] The remaining weak peak is assigned to the hydroxy group stretching from surface phosphate groups formed upon P doping and/or from water molecules adsorbed on the P-γ-Al_2O_3.[40] On the other hand, the weak peak with the high P doping level also suggested that either some of the phosphate groups were dehydrated and/or some of the phosphorus was incorporated into the lattice of Al_2O_3 (and not on the surface of the alumina). In the spectra of **OH-surf** model similar peaks, an intense peak around 2000 cm^{-1} as well as a relatively very small peak around 1650 cm^{-1}, are reproduced due to the asymmetric streching mode and inplane bending moments of O-H, respectively. A similar O-H bending mode is seen around 2200 cm^{-1} for **OH-md** model (see **Figure S12b**).

Indeed, a significant peak at 1100 cm^{-1} was shown up in P-γ-Al_2O_3, which was considered as the identification of different P-O stretching, especially for ideal tetrahedron $[PO_4]^{-3}$ groups. [43,12] However, our computational analysis shows that **OH-non-doped** model also indicates such a peak and the peaks in this region result from the O-H bending mode for OH-terminated surface models of P-γ-Al_2O_3. Only **O-sub** model has a peak due to P-O stretching in this region. For the other models, the vibrational modes of P appear between 800 and 1000 cm^{-1} as P-O bending mostly. This finding, in combination with the unexpected small peak of the hydroxy group of phosphate in the range of 3000-3800 cm^{-1}, supports our hypothesis that P is either in the form of surface phosphate groups, which did not carry hydrogen atoms, and/or some of P dopant incorporated inside the lattice or network of Al_2O_3.

It was reported that absorption in the range of 400-900 cm^{-1} corresponding to the Al–O stretching related to the octahedral (AlO_6) and tetrahedrons (AlO_4) units in the network of γ-Al_2O_3.[44] Both FT-IR spectra of γ-Al_2O_3 and P-γ-Al_2O_3 show absorptions in this range. More specifically, they all show peaks at 500 cm^{-1} and two shoulders at 720 and 776 cm^{-1}. The intensity of the peaks significantly decrease in P-γ-Al_2O_3, while the peak positions do not change very much. It was reported that Al-O stretching in AlO_6 and AlO_4 units were around 500-750 cm^{-1} and 750-850 cm^{-1}, respectively. The peak position may change significantly dependent on the fabrication methods and existence of defects and dopants in the lattice of γ-Al_2O_3.[45] On the other hand, Du et al. reported that the band at 523 and 570 cm^{-1} related to the stretching mode of Al–O in the AlO_6 and AlO_4, respectively. The bands at 734 and 774 cm^{-1} related to the symmetric stretching vibration of the AlO_4 tetrahedron.[44] Boumaza et al. reported that Al-O stretching in AlO_6 was 491 cm^{-1}.[46] Based on these literatures, the peak at 500 cm^{-1} is assigned for Al-O stretching in the octahedral units (AlO_6)[47,46] and the shoulders at 720 cm^{-1} and 776 cm^{-1} are related to the symmetric stretching vibration of the AlO_4 tetrahedron.[44,48] The relative decrease in these peaks upon P doping in this range might be due to the decrease of their population upon introducing phosphorus to the Al_2O_3 lattice or due to the formed PO_4 species covered on the surface, which decreases the detectable absorption of these bands. These results are confirmed by the presence of some P related vibrational modes seen at around 700 cm^{-1} and 500 cm^{-1} in both O/OH-terminated surface models. Overall, our computational approach is able to reproduce the main features of the experimental spectra, especially for **OH-sub** and **OH-surf** models.

CONCLUSIONS

In conclusion, employing experimental and computational methods, we have shown that the electronic properties of metal oxide surfaces can be manipulated via Group 5A doping (P atoms in this work). The surfaces can be made electron-rich in the sense that they have a lower work function than the undoped ones. The main reason for the work function lowering is the introduction of a surface dipole after doping. Interestingly, we find that the OH groups of thermodynamically stable mono- and bi-dentate Phosphate surface ligands cooperate with the surface by damping its dipole thereby decreasing the work function. Substitutional P-doping leads to nonsymmetric arrangements of P (tri- and four-coordinated) with an added dipole that once again dampens the work functions. The reduced coordination of the P atom correlates with the reported higher catalytic activity of P-doped alumina surfaces. With this study, we paved the way to using group 5A doping as a tuning knob for engineering electrostatic properties of metal oxide surfaces with catalytic applications.

MATERIALS AND METHODS

Preparation of samples. Doping γ-Al_2O_3 (Sigma Aldrich, gamma phase aluminum oxide nanopowder) with P was achieved by impregnation of γ-Al_2O_3 with phosphoric acid (with the ratio of 14g of γ-Al_2O_3 per 100mL of 1.0M phosphoric acid, Sigma Aldrich, 85 wt. % in H_2O) for 7 hrs while stirring to reach equilibrium adsorption.[49] After impregnation, the sample was dried at 100°C overnight, then it was placed in an oven at 550°C for 4.5 hrs. The product was then sonicated and dispersed in ultrapure water and centrifuged 5 times at 5,000 rpm for 8 mins, to make sure there is no free phosphoric acid in the sample. The final product was then dried at 100°C overnight.

Characterization. PF-KPFM measurements on the alumina samples were conducted with a Dimension ICON AFM setup inside an Argon-filled glove box where both H_2O and O_2 levels were below 0.1 ppm. The probes used were PFQNE-AL (Bruker AFM Probes), composed of a silicon nitride cantilever with a sharp silicon tip. The highly inert environment helped us to conduct more accurate measurements. P-γ-Al_2O_3 and γ-Al_2O_3 particles were first dispersed into ethanol, using bath sonication for 3 minutes. Then the samples were prepared by drop casting the dispersion of P-γ-Al_2O_3 and γ-Al_2O_3 particles onto a boron-doped silicon substrate. Solid state ^{27}Al (130.2 MHz) magic-angle spinning (MAS) NMR spectra were acquired at a magnetic field of 11.74T with a Bruker Avance III HD spectrometer equipped with a 4mm solid-state broadband probe (Bruker Biospin, Billerica, MA). One-pulse spectra were recorded with 45 deg pulse of 1 μs and 0.4 sec relaxation delay, collecting 1K data points over 104 KHz with the sample spinning at 10 KHz in a 4mm zirconia rotor, in which the finely powdered samples were packed. FT-IR spectra of γ-Al_2O_3 and P-γ-Al_2O_3 were acquired with a Thermo-Nicolet iS5 spectrometer (Thermo-Electron Corp., Madison, WI), using iD7 ATR accessory with diamond crystal plate, in the range of 400 to 4000 cm^{-1}. The spectra were recorded after 16 scans with a resolution of 4 cm^{-1}.

Computational Details. Our simulations relied on Density Functional Theory (DFT), and specifically we employ the Quantum ESPRESSO software.[50] In the calculations, the PBE functional[51] and Projector Augmented Wave (PAW) Pseudopotentials were employed with a kinetic energy cutoff of 50 Ry for the wavefunctions kinetic energy and 500 Ry kinetic energy cutoff for the charge density and potential. A Gaussian smearing to the occupations of the KS states was used, with a width (sigma) of 0.0001Ry. [50] The self-consistent field calculations featured a Broyden mixing beta of 0.15. A k-point sampling on a 2x2x1 grid of points for geometry optimizations and an 4x4x1 grid for all single-point computations were set.[52] Additional non-self consistent field (NSCF) was employed to generate smoother DOS plots.

The NMR calculations were carried out on the optimized bulk γ- Al_2O_3 structures by first performing a self consistent field (SCF) calculation with pw.x. Computation of NMR spectra have been carried out using DFT GIPAW (The Gauge-Including Projector Augmented Wave)[36] method using norm-conserving PPs (e.g. Al.pbe-tm-gipaw-dc.UPF) with the PBE functional.

IR spectra calculations were computed with PHONON[49] to generate vibrational frequencies carried out with fixed occupations (no smearing). In these calculations we first performed a SCF calculation with pw.x, second, we calculated the vibrational frequencies (normal modes/phonons) with ph.x and finally using dynmat.x we resolved the phonon information from ph.x output. The wavefunction kinetic energy cutoff for phonon calculation was 50 Ry on a 4x4x1 *k*-point grid with a 1.0×10^{-14} threshold.

The chemical potentials (μ) were calculated as follows:

For P-doped and surface models (**O-sub**, **O-surf**, **OH-sub**, and **OH-surf**):

$$\mu_{P-doped/surface} = E_{P\,doped-\gamma Al_2O_3} - E_{\gamma Al_2O_3} + (E_{\mathrm{Al}} - E_{\mathrm{P}}) \tag{1}$$

For monodentate (**O-md**, and **OH-md**) and bidentate models (**O-bd**, and **OH-bd**):

$$\mu_{monodentate} = E_{P\,doped-\gamma Al_2O_3} - E_{\gamma Al_2O_3} - E_{H3PO4} + E_H + E_O \tag{2}$$

$$\mu_{bidentate} = E_{P\,doped-\gamma Al_2O_3} - E_{\gamma Al_2O_3} - E_{H3PO4} + 2E_H + 2E_O \tag{3}$$

where the energy values were computed using the same cell for all species.

ACKNOWLEDGEMENTS

This material is based upon work supported by the National Science Foundation under Grant DMR-1742807. Work function studies with Kelvin Probe Microscope were supported by NSF MRI 1429062.

Supporting Information Available

Morphology and PDOS data of two P-doped models, as well as small cells and their computed IR spectra. Fundamentals of PF-KPFM technique and surface-averaged electrostatic potentials.

References

---

(1) Y.P. Gavin Chua, G.T. Kasun Kalhara Gunasooriya, M. Saeys, E.G. Seebauer, *J. Catal*., 2014, **311**, 306 – 313.
(2) L. Li, Y. Zhang, A.M. Schultz, X. Liu, P.A. Salvador, G.S. Rohrer, *Catal. Sci. Technol*., 2012**, 2**, 1945–1952.
(3) N.K. Nandakumar, E.G. Seebauer, *J. Phys. Chem. C*., 2014, **118**, 6873–6881.
(4) M. Chiesa, E. Giamello, D.M. Murphy, G. Pacchioni, M.C. Paganini, R. Soave, Z. Sojka, *J. Phys. Chem. B,* 2001, **105**, 497–505.
(5) P. Gorai, Y.V. Kondratenko, E.G. Seebauer, *J. Appl. Phys*., 2012, **111**(9), 094510.
(6) M.-G. Ma, Y.-J. Zhu, Z.-L. Xu, *Mater. Lett*., 2007, **61** (8), 1812-1815.
(7) Y. Rozita, R. Brydson, A.J. Scott, *J. Physics: Conference Series*, 2010, **241**(1), 012096.
(8) J.B. Peri, *J. Phys. Chem*., 1965, **69**, 220–230.
(9) W. Gu, M. Shen, X. Chang, Y. Wang, J. Wang, *J. Alloys Compd*., 2007, **441**, 311–316.
(10) Y. Wang, J. Wang, M. Shen, W. Wang, *J. Alloys Compd.,* 2009, **467**, 405–412.
(11) J. Wang, Y. Wang, J. Wen, M. Shen, W. Wang, *Microporous Mesoporous Mater*., 2009, **121**, 208–218.
(12) G.H. Mekhemer, A.K.H. Nohman, N.E. Fouad, H. Khalaf, *Colloids Surfaces A Physicochem. Eng. Asp*., 2000, **161**, 439–446.
(13) G. Busca, G. Ramis, V. Lorenzelli, P.F. Rossi, A. La Ginestra, D. Chimica, R. La, P.A. Mor, P. Patron, *Langmuir* 1989, **5**, 911–916.
(14) P. Da Costa, C. Potvin, J.M. Manoli, M. Breysse, G. Djéga-Mariadassou, *Catal. Letters* 2001, **72**, 91–97.
(15) K. Gishti, A. Iannibello, S. Marengo, G. Morelli, P. Tittarelli, V. Bassini, *Appl. Catal*. 1984, **12**, 381–393.
(16) K.H. Zum Gahr, *Wear* 1996, **200**, 215–224.
(17) H.R. Pasaribu, J.W. Sloetjes, D.J. Schipper, *Wear* 2003, **255**, 699–707.
(18) T. Ishizaka, R. Nozaki, Y. Kurokawa, *J. Physical Chemistry of Solids* 2002, **63**, 613–617.
(19) O. Ozuna, G.A. Hirata, J. McKittrick, *Appl. Phys. Letters* 2004, **84**, 1296–1298.
(20) J. Zhang, Y. Wu, M. Xing, S.A.K. Leghari, S. Sajjad, *Energy Environ. Sci*. 2010, **3**, 715–726.
(21) Li, R.; Wei, Z.; Gou, X.; Xu, W. *RSC Adv*. 2013, 3, 9978-9984.
(22) C.H. Choi, M.W. Chung, S.H. Park, S.I. Woo, *Phys. Chem. Chem. Phys*. 2013, **15**, 1802–1805.
(23) A.K. Khattak, K. Mahmood, M. Afzal, M. Saleem, R. Qadeer, *Colloids Surfaces A: Physicochem. Eng. Asp*. 2004, **236**, 103–110.
(24) M. Villarroel, P. Baeza, F. Gracia, N. Escalona, P. Avila, F.G. Gil-Llambias, *Applied Catalysis A* 2009, **364**, 75–79.
(25) J. Quartararo, J.P. Amoureux, J. Grimblot, *J. Molecular Catal. A* 2000, **162**, 353–365.
(26) G. Gutiérrez, A. Taga, B. Johansson, *Phys. Rev. B* 2001, **65**, 012101–1.
(27) H.P. Pinto, R.M. Nieminen, S.D. Elliott, *Phys. Rev. B* 2004, **70**, 125402-1.
(28) T. Taniike, M. Tada, Y. Morikawa, T. Sasaki, Y. Iwasawa, *J. Phys. Chem. B* 2006, **110**, 4929–4936.
(29) G. Paglia, C.E. Buckley, A.L. Rohl, R.D. Hart, K. Winter, A.J. Studer, B. Hunter, J.V. Hanna, *Chem. Mater*. 2004, **16**, 220–236.
(30) M. Cococcioni, S. de Gironcoli, *Phys. Rev. B* 2005, **71**, 035105.
(31) E. Finazzi, C. Di Valentin, G. Pacchioni, A. Selloni, *J. Chem. Phys*. 2008, **129**, 154113.

---

(32) D. Cornil, H. Li, C. Wood, G. Pourtois, J. Brédas, J. Cornil, *ChemPhysChem* 2013, **14**, 2939-2946.

(33) M. Acikgoz, J. Harrell, M. Pavanello, *J. Phys. Chem. C* 2018, **122** (44), 25314-25330.

(34) N.S. Barrow, A. Scullard, N. Collis, *Johnson Matthey Technol. Rev.* 2016, **60**, (2), 90.

(35) L. Samain, A. Jaworski, M. Edén, D.M. Ladd, D.K. Seo, F. Javier Garcia-Garcia, U. Häussermann, *J. Solid State Chemistry* 2014, **217**, 1-8.

(36) J.R. Yates, C.J. Pickard, F. Mauri, *Phys. Rev. B* 2007, **76**, 024401.

(37) R. Wischert, P. Florian, C. Copéret, D. Massiot, P. Sautet, *J. Phys. Chem. C* 2014, **118**(28), 15292–15299.

(38) S. Wang, X. Li, S. Wang, Y. Li, Y. Zhai, *Mater. Lett.* 2008, **62** (20), 3552-3554.

(39) H.A. Dabbagh, M. Yalfani, B.H. Davis, *J. Mol. Catal. A: Chemical* 2005, **238** (1), 72-77.

(40) E.C. Decanio, J.C. Edwards, T.R. Scalzo, D.A. Storm, J.W. Bruno, *J. Catal*. 1991, **132** (2), 498-511.

(41) S. Sigurdson, V. Sundaramurthy, A.K. Dalai, J. Adjaye, *J. Mol. Catal. A: Chemical* 2008, **291** (1), 30-37.

(42) Meher, T.; Basu, A. K.; Ghatak, S., *Ceramics International* 2005, 31 (6), 831-838.

(43) M. Rokita, M. Handke, W. Mozgawa, *Journal of Molecular Structure* 1998, **450** (1), 213-217.

(44) X. Du, Y. Wang, X. Su, J. Li, *Powder Technology* 2009, **192** (1), 40-46.

(45) R. Rinaldi, U. Schuchardt, *J. Catal*. 2005, **236** (2), 335-345.

(46) A. Boumaza, L. Favaro, J. Lédion, G. Sattonnay, J.B. Brubach, P. Berthet, A.M. Huntz, P. Roy, R. Tétot, *J Solid State Chem.* 2009, **182** (5), 1171-1176.

(47) M.N. Barroso, M.F. Gomez, L.A. Arrúa, M.C. Abello, *Catal. Letters* 2006, **109** (1), 13-19.

(48) X.L. Qi, Z. Wang, S.J. Li, B. Li, X.Y. Liu, B.X. Lin, *Acta Physico - Chimica Sinica* 2006, **22** (2), 198-202.

(49) R. Iwamoto, J. Grimblot, *Adv. Catal.* 1999, **44**, 417–503.

(50) P. Giannozzi, S. Baroni, N. Bonini, M. Calandra, R. Car, C. Cavazzoni, D. Ceresoli, G.L. Chiarotti, M. Cococcioni, I. Dabo, A. Dal Corso, S. de Gironcoli, S. Fabris, G. Fratesi, R. Gebauer, U. Gerstmann, C. Gougoussis, A. Kokalj, M. Lazzeri, L. Martin-Samos, N. Marzari, F. Mauri, R. Mazzarello, S. Paolini, A. Pasquarello, L. Paulatto, C. Sbraccia, S. Scandolo, G. Sclauzero, A.P. Seitsonen, A. Smogunov, P. Umari, R.M. Wentzcovitch, *J. Phys. Condens. Matter* 2009, **21**, 395502.

(51) J.P. Perdew, K. Burke, M. Ernzerhof, *Phys. Rev. Lett.* 1996, **77** (18), 3865–3868.

(52) H.J. Monkhorst, J.D. Pack, *Phys. Rev. B* 1976, **13**, 5188.